Received: 26 August 2020 | Accepted: 26 December 2020

DOI: 10.1002/eom2.12077

REVIEW

EcoMat FUNCTIONAL MATERIALS FOR GREEN ENERGY AND ENVIRONMENT WILEY

Reality or fantasy—Perovskite semiconductor laser diodes

Wei Gao[1,2] | **Siu Fung Yu**[1,2]

[1]Department of Applied Physics, The Hong Kong Polytechnic University, Kowloon, Hong Kong, People's Republic of China

[2]Shenzhen Research Institute, The Hong Kong Polytechnic University, Shenzhen, People's Republic of China

Correspondence
Siu Fung Yu, Department of Applied Physics, The Hong Kong Polytechnic University, Hung Hom, Kowloon, Hong Kong, People's Republic of China.
Email: sfyu21@hotmail.com

Funding information
Hong Kong Polytechnic University, Grant/Award Numbers: 1-BBA5, 1-ZVGH, BCEE, G-YBHG; National Natural Science Foundation of China, Grant/Award Number: 61775187

Abstract

Perovskite semiconductor has emerged as a promising laser gain medium; however, it is still a challenge to fabricate electrically pumped perovskite lasers due to the insufficient electrical-to-optical conversion efficiency. Here, the current progress on the lasing performance of optically pumped perovskite lasers is reviewed. The advancement in the control of carrier transport and recombination properties of perovskite light-emitting diode architectures is also studied. Hence, the obstacles preventing the fabrication of perovskite laser diodes are investigated. More importantly, a strategy toward electrically driven perovskite lasers is proposed base on the successful development of organic semiconductor laser diodes.

KEYWORDS

electrically pumped lasers, light-emitting diodes, perovskite lasers, perovskite semiconductors

1 | INTRODUCTION

Although halide perovskites were synthesized 120 years ago,[1] they started to receive attention in the late 1990s after showing their prospective optoelectronic properties.[2-5] This is because of their excellent electrical characteristics include low trap-state densities[6] and low recombination rate of electrons and holes when compare to that of the III-V semiconductor materials.[7-10] They also have large carriers' mobility[11] which is critically important to the operation of electronic devices. Moreover, the direct bandgap behavior with strong band edge absorption guarantees their excellent optical properties.[12] Hence, the use of halide perovskites has led to the fabrication of high-performance solar cells,[13,14] photodetectors,[15] and light-emitting diodes (LEDs).[16] On the other hand, it is noted that the cations of perovskites can be replaced by other organic or inorganic cations to tune the bandgap energy through the change of lattice constants.[17] The dimensionality reduction of halide perovskites, which can lead to an increase of exciton binding energy, supports the generation of strong excitonic gain at a high operating temperature.[6,18,19] Therefore, these indicate that the halide perovskite semiconductors are also a promising laser gain medium. Eventually, the first hybrid perovskite semiconductor laser has been realized in 2014.[20] Subsequently, studies of hybrid and all-inorganic perovskite semiconductors had demonstrated lasing emission at room temperature over the entire visible spectrum.[21,22] Unfortunately, all these perovskite lasers are optically pumped and it remains a challenge today to achieve lasing emission under electrical driven.

The first step toward electrically pumped perovskite lasers is to minimize the corresponding excitation threshold through the appropriate design of gain material compositions and resonators.[23] For example, methylammonium lead bromide ($MAPbBr_3$) perovskite

thin-film semiconductor laser with distributed feedback (DFB) structure is realized to sustain lasing emission at temperature up to 100°C with a low threshold of 3.4 μJ/cm^2 under optical pulses excitation (@532 nm, 0.3 ns, 1 kHz).[24] The synthesis of single-crystalline cesium lead bromide ($CsPbBr_3$) perovskites nanowires (NWs) is another effective approach to secure room-temperature operation with a low threshold of 3 μJ/cm^2 (@355 nm, 150 fs, 100 kHz). This is because of the high-crystal quality of the gain medium and the defect-free Fabry Perot resonator with extremely low cavity losses.[25] The lowest threshold of single-crystalline halide perovskites ($MAPbX_3$ for X = I, Br, and Cl) NWs is recorded to be 0.22 μJ/cm^2 (@805 nm, 100 fs, 250 kHz) at room temperature.[26] Nevertheless, these perovskite semiconductor lasers are operated under short optical pulses excitation. On the other hand, continuous-wave (CW) operation perovskite laser is achieved by using $MAPbI_3$ perovskite semiconductor as the active layer of a DFB resonator. The laser operating at or below 160 K (ie, below the tetragonal-to-orthorhombic phase transition temperature) with an excitation threshold of 17 kW/cm^2.[27] Higher operation temperature can also be obtained by using mixed cation perovskite to suppress the phase change due to the increase of temperature.[28] Furthermore, the solution-processed $CsPbBr_3$ perovskite NWs are utilized to realize CW operation via polariton lasing at cryogenic temperature (77 K) with an excitation threshold of 6 kW/cm^2.[29] Moreover, the development of room-temperature $MAPbI_3$ perovskite DFB lasers has shown a low threshold of 13 W/cm^2 under CW operation which is due to the extra-low cavity losses of the DFB resonator.[30] The current fabrication of vertical-cavity surface-emitting laser (VCSEL) using a 1 μm thick $MAPbBr_3$ perovskite as the active layer has demonstrated an ultralow threshold of 34 mW/cm^2 at room temperature under CW operation.[31] This may be due to the ultralow cavity losses of the microcavity with Bragg reflectivity as high as 99.9% at the lasing wavelength. On the other hand, formamidinium lead bromide ($FAPbBr_3$)-based quasi-2D perovskites (ie, thickness of ~100 nm) are proposed as the gain medium of DFB resonators to realize green room-temperature CW lasing with excitation threshold of 45 W/cm^2.[32] It is shown that the reason to achieve high optical gain is the suppression of long-lived triplet excitons.

Table 1 summarizes the recent progress on the development of optically pumped perovskite semiconductor lasers and their related lasing characteristics. The fourth column of the table shows the excitation methods of the lasers, while the sixth column indicates the excitation threshold. Either pulse energy (for pulses excitation), optical power (for CW excitation), or both are given as the excitation threshold of the lasers. The average power, P_{ave}, of the excitation pulses is also indicated in the column. It is observed that the threshold of the excitation pulses reduces from P_{ave} of 0.75 W/cm^2 (fs pulses)[25] to 4 mW/cm^2 (ns pulses)[31] and the threshold for the perovskite laser under CW operation significantly reduces from 17 kW/cm^2[27] to 34 mW/cm^2[31] for the past 5 years of progress. This is attributed to the improvement in the fabrication of high-quality perovskite semiconductors, which can reduce the internal absorption losses and enhance the optical gain. Further careful design of laser cavities with strong optical confinement (ie, laser cavity with a high Q-factor such as DFB and VCSEL) leads to ultralow cavity losses. As a result, an ultralow excitation threshold, which suppresses the thermal and optical degeneration of the optical gain arisen from the pump induced heating and the accumulation of photo-induced defects, respectively,[39] is obtained to support CW operation at room temperature.

For the VCSEL,[31] it is noted that the excitation threshold under pulses and CW operation is found to be 4 μJ/cm^2 (ie, 500 W/cm^2) and 34 mW/cm^2, respectively. The lasers under pulses excitation require higher peak power so that the overall generated carrier concentration can be higher than that of the average threshold value. Hence, the threshold of the same device under CW operation is lower than the peak power of the pulses. On the other hand, the time-average power of the pulses (ie, P_{ave} of 4 mW/cm^2) is much less than its CW excitation threshold so that the heating effect is significantly reduced in pulses operation. The eighth column of the table projects the equivalent threshold current of the lasers under electrical pulses and CW operation (see Appendix for the calculation). The equivalent excitation threshold of VCSEL under nanosecond pulses and CW operation are estimated to be 314 A/cm^2 and 24 mA/cm^2, respectively. In the calculation, the influence of Joule heating and other heating effects are ignored. Now, the question is whether these lasers can be electrically excited by using the available perovskite LED architectures as the carrier injection media. Hence, it is necessary to study the process of achieving electrically pumped organic lasers by using organic LED architectures, which have similar carrier transport layers (CTLs) to that of the perovskite LEDs, to inject carriers.

2 | DOES ANYTHING LEARN FROM THE ELECTRICALLY DRIVEN ORGANIC LASERS?

After the demonstration of optically pumped organic solid-state semiconductor lasers in 1996,[40] extensive investigations have concentrated on the realization of electrically

TABLE 1 Recent progress of optically pumped perovskite semiconductor lasers

Materials	Feedback mechanism	Lasing λ (nm)	Excitation method	Temp.	Threshold (P_{ave} of pulses)[a]	Active layer thickness	Threshold current[b]	Year
$MAPbI_3$ TF[20]	ASE	680	150 fs, 600 nm, 1 kHz	RT	12 $\mu J/cm^2$ (12 mW/cm^2)	65 nm		2014
$CsPbBr_3$ QD[33]	WGM	524.5	5 ns, 400 nm, 20 Hz	10 K	11.5 mJ/cm^2 (0.22 W/cm^2)	in solution		2015
$MAPbI_3$ NW[26]	FP	787	150 fs, 402 nm, 250 kHz	RT	0.22 $\mu J/cm^2$ (55 mW/cm^2)	~200 nm	1 MA/cm^2	2015
$CsPbBr_3$ NW[34]	FP	530	150 fs, 402 nm, 250 kHz	RT	2.8 $\mu J/cm^2$ (0.7 W/cm^2)	700 nm		2016
$CsPbBr_3$ NW[25]	FP	530	150 fs, 355 nm, 250 kHz	RT	3 $\mu J/cm^2$ (0.75 W/cm^2)	300 nm		2016
$MAPbI_3$ TF[35]	VCSEL	778	0.34 ns, 532 nm, 1 kHz	RT	7.6 $\mu J/cm^2$ (7.6 mW/cm^2)	~305 nm	17.6 kA/cm^2	2017
$MAPbBr_3$ TF[24]	DFB	555	0.3 ns, 532 nm, 1 kHz	RT	3.4 $\mu J/cm^2$ (3.4 mW/cm^2)	~200 nm	7.5 kA/cm^2	2018
$MAPbI_3$ TF[27]	DFB	785	CW, 445 nm	102 K	17 kW/cm^2	120 nm		2017
$MAPbI_3$ TF[36]	DFB ASE	813	CW, 355 nm	RT	0.1 W/cm^2	160 + 70 nm[c]	63 mA/cm^2	2018
$CsPbBr_3$ NW[37]	FP	524	CW, 405 nm	4 K	1.45 nW	~280 nm		2018
			35 fs, 400 nm, 1 kHz		12.3 $\mu J/cm^2$ (12.3 mW/cm^2)			
$CsPbBr_3$ NW[29]	Polariton	533	CW, 450 nm	77 K	6 kW/cm^2	~300 nm		2018
$MAPbI_3$ TF[30]	DFB	807	CW, 355 nm	RT	13 W/cm^2	145 + 30 nm[c]	8.17 A/cm^2	2018
$Cs_{0.1}(MA_{0.17}FA_{0.83})_{0.9}Pb_{0.84}(I_{0.84}Br_{0.16})_{2.68}$ TF[28]	ASE	790	CW, 532 nm	80 K	387 W/cm^2	~185 nm		2019
$MAPbBr_3$ QD[38]	DFB	539	CW, 405 nm	RT	15 W/cm^2	300 + 700 nm[c]	10.7 A/cm^2	2019
$MAPbBr_3$ TF[31]	VCSEL	565	CW, 405 nm	RT	34 mW/cm^2	1 μm	24 mA/cm^2	2019
			8 ns, 355 nm, 1 kHz		4 $\mu J/cm^2$ (4 mW/cm^2)		314 A/cm^2	
$FAPbBr_3$ q2DF[32]	DFB	~553	CW, 488 nm	RT	45 W/cm^2	~100 nm	38.8 A/cm^2	2020
	ASE	~550	3 ns, 337 nm, 20 Hz		16.7 $\mu J/cm^2$ (0.33 mW/cm^2)		3.3 kA/cm^2	

Abbreviations: ASE, amplified spontaneous emission; DFB, distributed feedback; FP, Fabry-Pérot; NW, nanowire; q2DF, quasi-2D film; QD, quantum dots; RT, room temperature; TF, thin film; VCSEL, vertical-cavity surface-emitting laser; WGM, whispering gallery mode.

[a] P_{ave} = pulse energy × frequency (ie, average power of the pulses).

[b] Equivalent peak and average injection current density (see Appendix).

[c] $h_1 + h_2$ (h_1—grating height, h_2—perovskite residue thickness).

pumped organic semiconductor lasers. This is the goal of organic laser industries that flexible and compact laser diodes can be fabricated by a low-cost roll-to-roll solution-based process and this is also the reason to develop perovskite semiconductor lasers. Previously, researchers have made use of the electrical injection architectures of organic LEDs and collaborated with optical waveguides/resonators which having spectral filtering properties to achieve "so call" electrically pumped organic lasers. For example, an asymmetric slab waveguide, which supporting resonant leaky mode at a cutoff wavelength, is used to obtain the narrowing of the electroluminescence spectrum.[41] On the other hand, a $\lambda/2$ microcavity—a Fabry-Pérot interferometer with high mirror reflectivity (>99%) is applied to support the narrowing of emission linewidth.[42] However, the operation principle of these devices is equivalent to organic LED integrated with a laser line filter so that their emission characteristics do not satisfy the claim of lasing. Therefore, we should avoid making the same mistake during the development of electrically pumped perovskite lasers.

In general, conventional lasing arises from the amplification of spontaneous emission and the coherent optical feedback within the gain medium of a resonator. Hence, the laser beam has spatial and temporal coherence and is strongly polarized. To verify the support of conventional lasing from electrically pumped resonators, it is necessary to demonstrate unambiguously:

- the presence of the threshold—the slope efficiency of the output power shows an abruptly change during the increase of injection current (see Figure 1A);
- the narrowing of emission spectrum above the threshold (ie, due to the requirement of phase coherence of the lasing light, the corresponding spectrum linewidth above the threshold should be <0.2 nm, see Figure 1A);
- the spatial coherence of the laser beam (ie, a speckle pattern can be observed by illuminating a coherent laser beam on a rough surface, see Figure 1B);
- and the strongly linear polarization of the lasing beam above threshold (ie, emitted light varies from unpolarization below to strongly linearly polarized above the threshold).

Hence, to claim a light-emitting device is a conventional laser, its output characteristics should satisfy the above requirements simultaneously. The previously reported electrically pumped organic lasers although show linewidth narrowing, the "lasing linewidth" is too large (ie, >1.9 nm)[42] to be phase coherence so that they are not a "laser."

What is unconventional laser—polariton laser?[43] The main difference between a conventional laser and a polariton laser is that the latter case requires no population inversion. Coherent light is generated from the steady-state leakage of an exciton-polariton condensate below the threshold for population inversion. For an ideal polariton laser, there will be no threshold except at a very high excitation power. However, in a normal situation, the polariton lasers will have two excitation thresholds. The first threshold at a lower excitation power is for polariton lasing—we should observe spatial coherence and polarization characteristics of the laser beam. The second threshold at a higher excitation power (ie, an order of magnitude higher than the first threshold) is for conventional lasing—the output characteristics should show the signatures of conventional lasing.

It is believed that the difficulties to realize organic lasers under electrical excitation are due to (a) poor net optical gain of the organic materials and (b) inappropriate design of the laser structure.[40] First, the organic materials, which have low stimulated emission cross section (ie, optical gain) and the emission light wavelength overlaps with the triplet excitons and polarons absorption peaks under electrical excitation, have low net optical gain. Second, due to the low mobility (ie, high resistivity) of the organic materials, it is necessary to place the metallic electrodes very close to the active layer

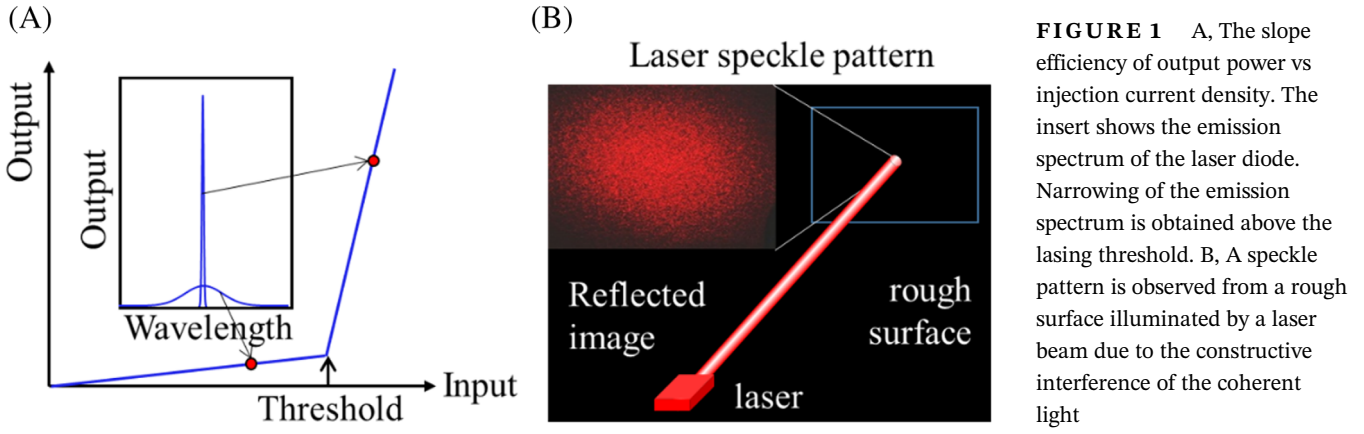

FIGURE 1 A, The slope efficiency of output power vs injection current density. The insert shows the emission spectrum of the laser diode. Narrowing of the emission spectrum is obtained above the lasing threshold. B, A speckle pattern is observed from a rough surface illuminated by a laser beam due to the constructive interference of the coherent light

of the resonators. As a result, the optical modes are strongly absorbed by the metallic electrodes so that high cavity losses are unavoidable. Hence, these are the main difficulties preventing us to obtain "truly" electrically pumped organic lasers.

After the observation of room-temperature lasing from an optically pumped organic laser with a threshold of either 0.09 μJ/cm^2 @20 Hz excited by 337 nm 800 ps optical pulses (ie, equivalent threshold current is ~61 A/cm^2 if $\alpha \sim 1.5 \times 10^6$ cm^{-1} is assumed) or 0.06 μJ/cm^2 @10 kHz excited by 365 nm 10 ps optical pulses (ie, ~3.5k A/cm^2) in 2017,[44] an electrically pumped distributed feedback organic diode was achieved 2 years later.[45] This is verified by showing unambiguously the signatures of conventional lasing including a clear lasing threshold, linewidth narrowing, and strong polarization dependence. The laser is operating at room temperature under electrical pulses excitation (400 ns, 1 kHz) with a threshold current of ~700 A/cm^2. The main reasons to obtain lasing are (a) the selection of a high net gain organic semiconductor and (b) the extremely low-loss resonator design under external injection of carriers. In the fabrication of the resonator, 4,4′-bis[(*N*-carbazole)styryl] biphenyl (BSBCz) thin film is used to generate high net optical gain under electrical excitation. This is possible as the lasing wavelength is spectrally separated from the triplet-exciton and polaron absorption peaks by using rectangular gratings with appropriate reflection wavelength. Furthermore, the design of the rectangular gratings using SiO_2 dielectric suppresses the light absorption at the metallic electrodes as well as allows the effective injection of carriers into the Cs:BSBCz active layer for achieving higher optical gain, see Figure 2A. Here, the architecture design minimizes the number of organic hetero-interfaces so that the accumulation of charges as well as the internal losses of the laser cavity can be suppressed under the injection of high current densities. As a result, the corresponding injection efficiency has been improved over the conventional design of organic LEDs. Besides, the emission

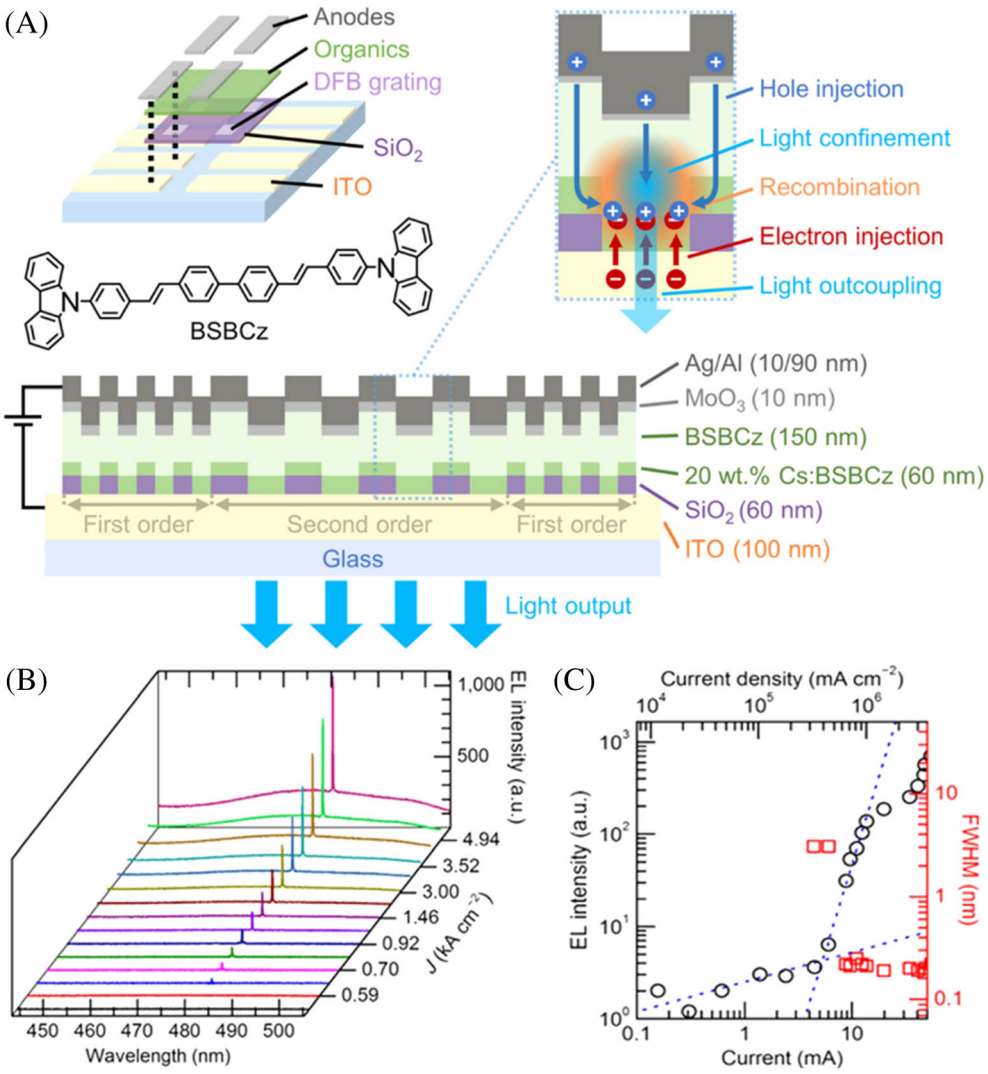

FIGURE 2 A, Schematic representation of the organic laser diode. B, Emission spectra of an organic laser diode collected in the direction normal to the substrate plane for different injected current densities. C, Output intensity and full width at half maximum (FWHM) of the emission spectra as a function of the current. Reproduced with permission: Copyright 2019, The Japan Society of Applied Physics[45]

characteristics unambiguously fulfill the claim of "lasing," see Figure 2B,C. On the other hand, thermal degeneration is still the main problem of the electrically pumped organic lasers as strong efficiency roll-off occurs for the injection pulses larger than 2.2 kA/cm^2. The influence of thermal degeneration (ie, intrinsic properties of organic materials) is still the remaining challenge to achieve organic semiconductor laser diodes under CW operation at room temperature.

Table 2 shows the physical and electrical properties of some semiconductor materials. It is noted that the low melting point of perovskite semiconductors has the advantage to fabricate light-emitting devices at a low cost. Furthermore, due to the short thermal response time (ie, $\propto \kappa_m C_p$), the dissipation of heat from the perovskite semiconductors is relatively faster than that of the organic materials. Hence, the physical properties of halide perovskite semiconductors are compatible with or better than that of BSBCz. On the other hand, the electrons and holes mobilities of the halide perovskite semiconductors, which are compatible with that of III-V semiconductor materials, are higher than that of the BSBCz. Besides, perovskite single crystals offer even lower bulk defect densities of 10^9 to 10^{11} cm^{-3}. Therefore, these indicate that the electrical properties of halide perovskite semiconductors are suitable for the realization of high-performance electronic devices. Furthermore, the optical gain of perovskite semiconductors, which have a direct bandgap with minimal charge-trapping defects supporting band-to-band radiative recombination, can be as high as ~3×10^3 cm^{-2}.[69] This value is compatible with that of single-crystal GaAs and higher than that of the BSBCz (ie, the radiative decay time of BSBCz is ~10^9 seconds^{-1} or equivalent optical gain of ~8 cm^{-1} at threshold[70]). Therefore, the optical characteristics of perovskite semiconductors should be favorable for laser applications. As the architecture design of the organic laser diode shown in Figure 2 can provide injection pulses with a peak value of few kA/cm^2 which may be sufficient to drive some of the perovskite lasers shown in Table 1,[24,31] therefore, it is expected with a high chance to realize electrically pumped perovskite lasers.

To the best of our understanding, electrically pumped perovskite lasers have yet to be demonstrated. So, what are remained obstacles required to be overcome before the successful fabrication of perovskite laser diodes? First of all, there is no suitable architecture of injection/transport layers available to achieve effective injection of carriers into the perovskite emitting layer. Furthermore, the heating effect, which arises from the low conversion efficiency of the external carrier injection, significantly deteriorates the optical gain of the perovskite semiconductors. Hence, these may be the main reasons for dragging the development of electrically pumped perovskite lasers. As we know that the key to obtaining organic lasers is to deduce the suitable injection architecture for maximizing the conversion efficiency of the laser diode under high current injection, therefore, it is necessary to investigate the carrier transport process causing the low conversion efficiency of the available perovskite LED architectures.

3 | CARRIER TRANSPORT AND RECOMBINATION PROPERTIES OF PEROVSKITE LED ARCHITECTURES

Figure 3 shows the schematic diagram of a standard three-layer architecture under the external injection of carriers. The device consists of an anode, a hole-transport layer (HTL), a halide perovskite emitting layer, an electron-transport layer (ETL), and a cathode. The ideal HTL is also an electron blocking layer (EBL) to block excessive electrons. Similarly, the ETL is also expected as a hole blocking layer (HBL) to block excessive holes. It is believed that (a) charge carrier injection imbalance, (b) overflow of carriers, (c) electric field inside the emitting layer, (d) nonradiative recombination, and (e) Joule heating are the potential mechanisms affecting the conversion efficiency of the standard three-layer LED architecture.

3.1 | Charge carrier injection imbalance

The existence of charge injection barriers between the perovskite emitting layer and CTLs leads to the imbalanced injection of electrons and holes. This inefficient injection of carriers, which is a critical problem needed to be addressed to realize electrically pumped perovskite lasers, causes low electroluminescence performance[46,78] and a high turn-on voltage (V_{on}) in the perovskite LEDs.[77,79] Therefore, the electrical properties of the adjacent CLTs, especially the underlayer on which the perovskite emitting layer is deposited, play a crucial role of charge injection efficiency. A prevalent strategy to overcome this issue is to introduce various types of organic materials or metal-doped semiconductors to reduce the injection barriers, improve charge-transporting ability and balance injected charges. Herein, some successful examples of CTL design in perovskite LEDs are reviewed, and these approaches may be utilized to achieve perovskite laser diodes.

TABLE 2 Physical and electrical properties of semiconductors

Materials	Melting point (°C)	Thermal conductivity, κ_m (W/m·K @RT)	Specific heat, C_p (J/kg·K)	Electron/hole mobility ($cm^2/V{\cdot}s$) (@RT)	Minor carrier lifetime (ns)	Intrinsic resistivity (Ω·m)	Intrinsic carrier conc. (cm^{-3})	Dielectric constant (@RT)
$CsPbX_3$	~580 X = I[46]	0.3 X = I 0.5 X = Cl	220 X = Cl	80-290/100-240[47]	1.3 X = Br[48]	2.1×10^{10} X = Br[48]	10^{15}-10^{17}[47]	4.1-4.5[a] X = Cl 3.2-5[a] X = Br 5-12.7[a] X = I
$MAPbI_3$	>200	1-3[49]	306[50]	197/136[51]	22[4]	~10^{104} ~10^{552} ~10^{953}	10^{16}-10^{18}[b]	~4.7-9 @visible[54]
$MAPbBr_3$	~220[46]	0.1-1.4	356[50]	20-60/20-60	41[4]	~10^8	5×10^9-5×10^{104}	~5.7@530 nm
BSBCz	~478[c]	0.2[44]	1400[44]	$3/7 \times 10^{-4}$[d] $0.4/1.2 \times 10^{-3}$[e]	~1.7[55]	~415[56]	2×10^{17}	4[57]
GaAs[58]	1240	~50	327	8000/400	~10	10^{10}	2.1×10^6	10.89
w-GaN	2900[59]	400[60]	490[60]	400/10^3[58]	6.5[61]	10^{62}	$3\text{-}6 \times 10^{19}$[62]	~7.1@370 nm[58]
w-ZnO	1977[63]	50[60]	494[60]	100-2000/5-30	1-2	2-5[64]	<10^6	~4.4@400 nm
Diamond[65]	4027	3320	519	4500/3800	6	>10^{15}	10^{-27}	5.7

Abbreviation: RT, room temperature.

[a]Static dielectric constant.[66]

[b]400 K.[49]

[c]Decomposition temperature, not melting point.[67]

[d]Under an electrical field of 2.5×10^4 V/cm.[68]

[e]Under 10^6 V/cm[57].

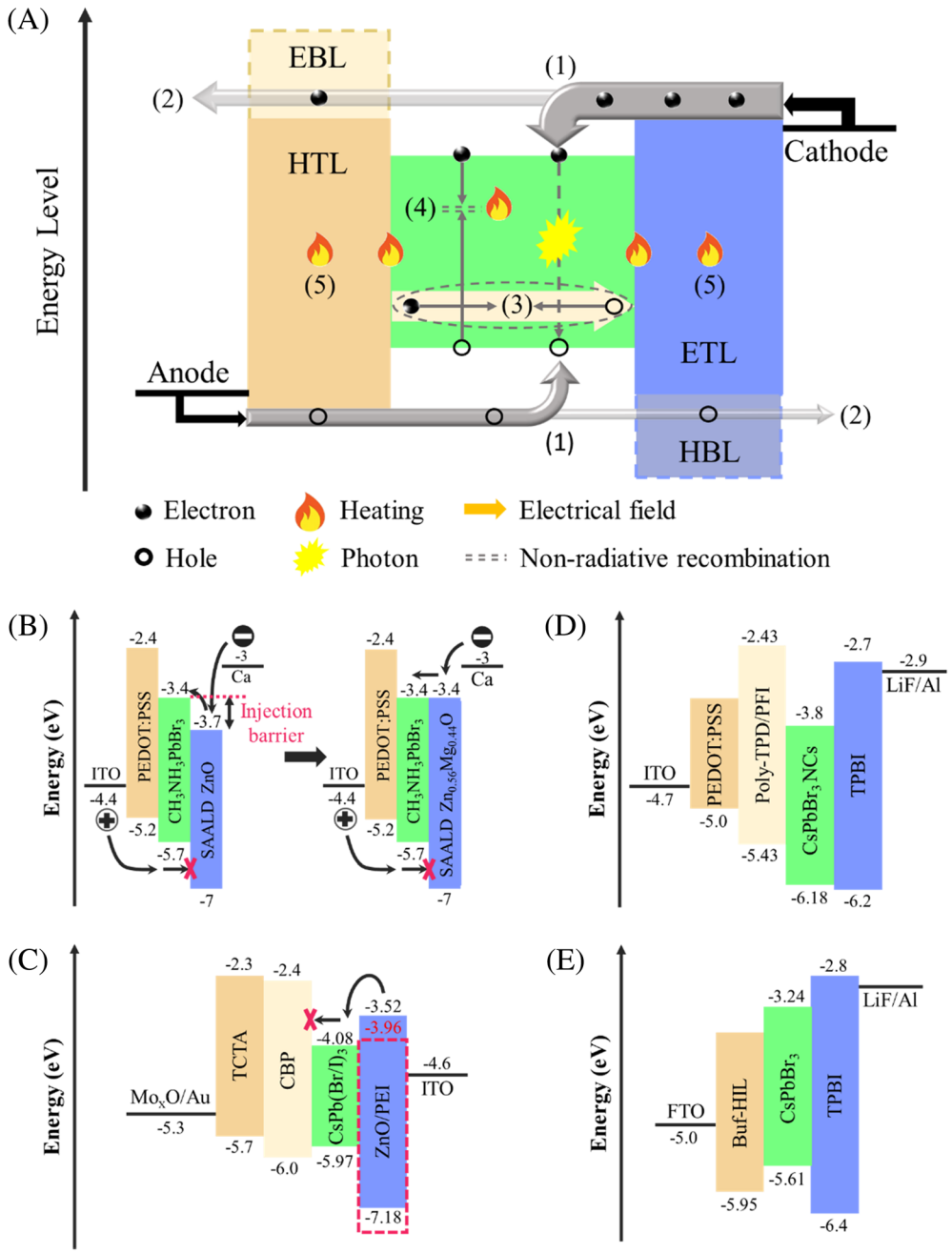

FIGURE 3 A, Schematic diagram of a standard three-layer light-emitting diode (LED) architecture under external injection of carriers. The factors affecting the corresponding quantum efficiency are (1) charge imbalance, (2) overflow of carriers, (3) electric field inside the emitting layer, (4) nonradiative recombination, and (5) Joule heating. B, Energy level diagram of perovskite light-emitting diodes (LEDs) with ZnO as an electron-transport layer (ETL). The diagram shows how to reduce an electron injection barrier with $MAPbBr_3$ by introducing ZnO as ETL while maintaining its function of blocking holes. Reproduced with permission: Copyright 2015, John Wiley & Sons.[71] C, The energy bands of ZnO and perovskite nanocrystal (NC) of $CsPb(Br/I)_3$ LED.[72] The red dash line represents the energy level of the ZnO NCs. Reproduced with permission: Copyright 2016, American Chemical Society.[73] D, Energy level diagram of poly-TPD and perovskite NC.[74-76] Reproduced with permission: Copyright 2016, American Chemical Society.[77] E, Energy level diagram of $CsPbBr_3$ LEDs with TPBI/CsPbBr3/Buf-HIL configuration. Reproduced with permission: Copyright 2017, John Wiley & Sons.[46] TCTA, 4,4′,4″-tris(carbazol-9-yl)triphenylamine; CBP, 4,4′-bis(carbazole-9-yl)biphenyl; PolyTPD, poly(4-butyltriphenylamine-4′,4″-diyl); TPBI, 1,3,5-tris(1-phenyl-1H-benzimidazol2-yl) benzene, Buf-HIL, PEDOT:PSS:PFI

The first room-temperature perovskite LED was demonstrated in 2014 but the corresponding external quantum efficiency (EQE) is very low due to the inefficient charge injection.[80] To address this issue, Mg-doped ZnO ($Zn_{1-x}Mg_xO$) was used to replace ZnO as an ETL,[81] and enable the drop of electron affinity from −3.7 to −3.4 eV

(Figure 3B) that was similar to that of perovskite materials. This barrier-free charge injection between ETL and the perovskite emitting layer provides a lower V_{on} and a narrower emission linewidth than that of the conventional InGaN LEDs.[71] The electron injection level of ZnO film could also be tuned by coating with polyethylenimine (PEI), which has been used to fabricate low work function electrodes in broad application fields.[79,82-84] Comparing with ZnO, the conduction band of ZnO/PEI can be reduced by 0.44 eV (Figure 3C), which enhances the electron injection within the device.[73]

An interfacial layer of perfluorinated ionomer (PFI) between the HTL and the perovskite nanocrystal emitting layer (Figure 3D) was proved to improve the hole injection efficiency.[77] This multilayered structure enables the valence band of HTL to increase to 0.34 eV, which results in efficient charge injection into the emitting layer and leads to three times enhancement of electroluminescence from $CsPbBr_3$ LEDs.[77] PFI was also used to modify poly (3,4-ethylenedioxythiophene):poly(styrene-sulfonate) (PEDOT:PSS) as an HTL to decrease the hole injection barrier with reduced work function (Figure 3E). This enhances the hole injection efficiency to improve the balance of electrons and holes so that a high electroluminescence intensity of 13 752 cd/m^2 with a pure emission spectrum of 16.5 nm can be obtained.[46]

The charge carrier mobility also plays an important role in the charge injection balance. For example, it is easy to realize charge injection balance in the LED architecture because the charge mobilities of HTL and ETL are both around 1×10^{-4} cm^2 V^{-1} s^{-1}.[77,85,86] Modifying the architecture of the emitting layer is also a new strategy to balance the charge injection. The quasi-core/shell structure, consisting of the bottom layer ($CsPbBr_3$/MABr) and top electrical passivating layer (MABr), can achieve a high initial EQE of 17% due to the balance of charge injection.[87]

3.2 | Overflow of carriers

Besides imbalanced charge injection, the low power conversion efficiency is also caused by the overflow of charge carriers, which leads to inefficient recombination of electrons and holes. CTL with a proper energy level of conduction or valence band is also used as the blocking layers to address this issue. For example, TiO_2 and poly (9,9′-dioctylfluorene) (F8) was utilized as an efficient HBL and EBL, respectively, to form a standard three-layer architecture $TiO_2/CH_3NH_3PbI_{3-x}Cl_x/F_8$ LED. HBL and EBL are used to confine injected charges inside the emitting layer to obtain effective light emission.[80] However, the similar energy level of the valance band of F8 and $MAPbBr_3$ makes F8 not a suitable charge blocking layer in this device. Hence, ZnO was used to replace F8 as a HBL to increase the energy level of the valance band. As a result, ZnO prevents the leakage of injected holes and supports efficiently radiative recombination in the perovskite emitting layer.[71] Alternatively, PEI can be used to modify ZnO (ie, a new PEI/ZnO layer) as a suitable HBL due to its deep valence-band energy level of −6.5 eV. Poly(9,9-dioctyl-fluorene-*co*-*N*-(4-butylphenyl) diphenylamine) with a low electron affinity (~2.1 eV) can also be utilized as an EBL to avoid carrier overflowing and allow strong confinement of carriers inside the emitting layer so that stable and efficient radiative recombination can be achieved.[79]

PEDOT:PSS has been successfully used as a traditional HTL in perovskite solar cells, but it is not suitable to use it alone as a HTL in LED due to its weak electron blocking effect.[88] Therefore, poly(9-vinlycarbazole) was employed as a blocking layer between HTL and perovskite QDs to overcome the drawback of PEDOT:PSS with shallow LUMO, resulting in blocking of injected electrons and obtaining efficient recombination of electrons and holes.[89] NiO_x was also used to replace PEDOT:PSS as an HTL because NiO_x exhibited a suitable energy level to block the electrons, while the TPBI was utilized to prevent the overflow of holes. As a result, the recombination probability of electrons and holes inside the emitting layer can be enhanced.[78]

In general, the suitable selection of potential barriers between CTLs and the emitting layer is the common strategy to suppress carrier injection imbalance and overflow from the perovskite LED architectures. Hence, charge carrier injection imbalance and charge overflow of carriers are solvable problems. Table 3 summarizes the recent progress of perovskite LEDs operating at room temperature.

3.3 | Electric field inside the emitting layer

Exciton-exciton annihilation, electric-field-induced dissociation of excitons into electron-hole pairs, and carrier-induced luminescence quenching are the possible mechanisms causing luminescence quenching under the influence of an electric field.[97-99] However, not all these mechanisms will appear simultaneously, and their attendance depends on the design of LEDs, dopant, and doping concentration of the emitting layer, and the magnitude of injection carrier densities. For example, the presence of exciton-exciton annihilation is strongly related to the amount of exciton density that can be obtained inside the emitting layer. This mechanism most likely occurs in perovskite polariton lasers especially

using multiple quantum wells (MQWs) perovskites as the emitting layer. This is because the exciton binding energy of perovskite MQWs can be as high as 360 meV,[100] and the condensation of excitons is required for achieving polariton lasing so that the chance to obtain exciton-exciton annihilation is high. As a result, the lasing threshold of polariton lasers can be significantly increased.[101] However, the influence of exciton-exciton annihilation in the conventional perovskite lasers is less important due to the Coulomb effects arisen from the high concentration of injected external carriers.

Electric field-induced exciton dissociation requires the presence of a high local field inside the emitting layer to separate excitons from electron-hole pairs. A halide perovskite $MAPbI_3$ layer sandwiched between two thick insulating polymer layers deposited with metal electrodes is used to investigate the influence of the internal electric field on the corresponding luminescence efficiency. It is found that the quenching factor of the devices can be larger than one if the applied electric field excesses 3.5×10^5 V/cm. As there is no flow of current across the device, the reduction of luminescence emission can be attributed to the separation of electrons and holes obtained from the ionization of photogenerated excitons.[102] This mechanism has also been observed from two-dimensional $(C_4H_9NH_3)_2PbI_4$[103] and $CsPbBr_3$ colloidal QDs perovskite thin-film.[104] Furthermore, MQW perovskite LED has observed PL quenching under the influence of field-induced charge separation, but this detrimental effect is less significant as the build-in electric field inside the emitting layer can be effectively reduced by the high forward bias voltage (ie, higher than its build-in potential).[105]

The decrease in luminescence under external injection of carriers is attributed to carrier-exciton interaction phenomena. The carriers can be either electrons or holes

TABLE 3 Summary of the electrical and optical properties of perovskite LEDs

Emitting layer	LED architecture EBL/EL/HBL or HTL/EL/ETL	λ_p (nm)	Luminance ($cd \cdot m^{-2}$)	EQE (%)	V_{on} (V)	CE (cd/A)	CD[a] (mA/cm^2)	Driven	Year
$MAPbBr_3$[80]	PEDOT:PSS/$MAPbBr_3$/F_8	517	364	0.1	3.3	0.3	120	CW	2014
$MAPbBr_3$[90]	Buf-HIL/$MAPbBr_3$/TPBI	543	417	0.13		0.58	90	CW	2015
$MAPbBr_3$[91]	SOCP/$MAPbBr_3$/TPBI	540	~15 000	8.53		42.9	34.9	CW	2015
$MAPbBr_3$[79]	TFB/$MAPbBr_3$/PEI:ZnO	532	20 000	0.8	2.2		~500	CW	2015
$MAPbBr_3$[78]	NiO_x/$MAPbBr_3$/TPBI	550	70 000		4.0	15.9	~400[b]	CW	2016
$CsPb(Br/I)_3$[73]	TCTA/CBP/$CsPb(Br/I)_3$/PEI:ZnO	648	2216	6.3	1.9	3.42	8	CW	2016
$CsPbBr_3$[46]	Buf-HIL/$CsPbBr_3$/TPBI	550	13 752	1.37		5.39	220	CW	2017
$CsPbBr_3$[87]	PEDOT:PSS/$CsPbBr_3$/$C_{37}H_{26}N_6$	525	14 000	20.3	2.7	78	~5	CW	2018
$CsPbBr_3$[92]	PEDOT:PSS/$CsPbBr_3$/TPBI	520	67 300	6.28	2.6	22.5	~100	CW	2018
$CsPbBr_3$[93]	PTAA/$CsPbBr_3$/TPBI	520	21 000	7.5	2.7	27	~70	CW	2020
$CsPbBr_3$[94]	PVK/$CsPbBr_3$/TPBI	514	2500	2.12	3.6	6.06	~5[b]	CW	2020
$MAPbI_{3-x}Cl_x$[80]	TiO_2/$MAPbI_{3-x}Cl_x$/F_8	754	6.8 $W \cdot sr^{-1} \cdot m^{-2}$	0.23	1.5		494	CW	2014
			13.2 $W \cdot sr^{-1} \cdot m^{-2}$	0.76			300[b]	1 ms, 100 Hz	
$MAPbI_{3-x}Cl_x$[79]	TFB/ $MAPbI_{3-x}Cl_x$/PEI:ZnO	768	28 $W \cdot sr^{-1} \cdot m^{-2}$	3.5	1.3		~160	CW	2015
$FAPbI_3$[95]	PEIE:ZnO/$FAPbI_3$/TFB	800	390 $W \cdot sr^{-1} \cdot m^{-2}$	20.7	1.3		18	CW	2018
$MAPbI_3$[96]	PolyTPD/$MAPbI_3$/$POPy_2$	750	2.6 $kW \cdot sr^{-1} \cdot m^{-2}$	17	2.0		~1 k	CW	2020
			59 $kW \cdot sr^{-1} \cdot m^{-2}$	1			750 k	250 ns	

Abbreviations: λ_p, peak wavelength of emission spectrum; CD, current density; CE, current efficiency; EL, emitting layer; EQE, external quantum efficiency; LED, light-emitting diode; SOCP:PEDOT:PSS, poly(3,4-ethylenedioxythiophene):poly(styrene-sulfonate); PEIE, polyethylenimine ethoxylated; PFI, perfluorinated ionomer; PTAA, (poly(bis(4-phenyl)(2,4,6-trimethylphenyl)amine)); $POPy_2$, phenyldi(pyren-2-yl)phosphine oxide; PTAA, (poly(bis(4-phenyl)(2,4,6-trimethylphenyl)amine)); PVK, poly(9-vinlycarbazole); TBAB, tetrabutylammonium bromide; TFB, poly(9,9-dioctyl-fluorene-*co*-*N*-(4-butylphenyl) diphenylamine); V_{on}, turn-on voltage.

[a]Current density at peak EQE.

[b]Current density at peak CE.

dependent on the carrier transportation mechanism and doping concentration of the emitting layer. For an organic LED with architecture supporting the transportation of electrons and has a buildup of electron density in the emitting layer, luminescence quenching will occur under external injection of electrons due to electron-exciton interaction. However, for another organic LED with standard three-layer architecture (ie, cathode/ETL/Alq_3/HTL/anode) under the influence of high electric field bias, no sight of either electric-field-induced or carrier-induced quenching is detected.[98] This is also true for a perovskite LED using the standard three-layer architecture (ie, cathode/ETL/$MAPbI_3$/HTL/anode).[106] Hence, this implies the quenching mechanisms triggering by the internal electric field inside the emitting layer can be avoided if the proper architecture of LEDs is adopted. Nevertheless, using $MAPbI_3$ as the emitting layer may lead to the slow redistribution of ionic charge, which is the dominant quenching mechanism of perovskite LEDs, changing the internal field profile and nonradiative trap concentration inside the emitting layer. Another investigation on the stability of perovskite solar cells has shown the deprotonation of organic cations by the trapped charge-induced local electric field at the interfaces between the emitting layer and CTLs.[107] Recent investigations have shown that the most problematic issue related to the electric field in perovskite devices is its stability. The decomposition of perovskite semiconductors may occur arising from the migration of ionic species/charged defects under the influence of the internal electric field.[108] Therefore, it seems that the influence of luminescence quenching (ie, arises from the electric field and external injection of carriers) may be less important than that of the stability of the $MAPbI_3$ emitting layer.

3.4 | Nonradiative recombination

Similar to the III-V semiconductors fabricated in their early development stage, nonradiative recombination processes observed from the perovskite semiconductors are dominated by their native defects.[109] This is because of the poor crystal quality so that point defects in the crystal lattice, surface pinholes generated from the high surface crystalline process rate, and surface defects at the grain boundaries are found from the perovskite thin films. In general, there are 12 native point defects in bulk $MAPbX_3$ containing the vacancies V_{MA}, V_{Pb}, and V_X, the interstitials MA_i, Pb_i, and X_i, and anti-site occupations MA_{Pb}, MA_X, Pb_{MA}, Pb_X, X_{MA}, and X_{Pb}.[110] However, only some of the point defects are predominant in the recombination process and their presence is dependent on the growth conditions and ingredients of the perovskite semiconductors. For example, defects of I_{Pb} and I_{MA} (ie, anti-site occupations of $MAPbI_3$) with transition energies of 0.6 and 0.75 eV below the conduction band (ie, deep trap levels) are obtained during the fabricated of $MAPbI_3$ films by one-step spin-coating and sequential deposition method, respectively.[111] The concentration of I_{Pb} and I_{MA}, which varies between 10^{14} and 10^{15} cm^{-3} at room temperature, is about one to two orders of magnitudes higher than that of high-crystal-quality GaAs semiconductors.[112] On the other hand, the surface mismatch between the CTLs and perovskite emitting layer generates interfacial defects which causing the annihilation of carriers and affecting the injection efficiency of the devices.

The existence of defects (ie, at the emitting layer and the interface between CTLs and emitting layer) creates defect energy states located within the energy bandgap of the perovskite semiconductors. Under forward bias, the injected carriers will be captured or trapped by these defect states. If the defect states have high activation energies (ie, at deep trap levels), the trapped carriers will be annihilated by recombining with the opposite carriers. This recombination process is mostly being nonradiative and accompanied by the emission of phonons. It is expected that the quantum efficiency of the perovskite LEDs reduces with the increase of the nonradiative recombination rate which is a function of defect concentration. As perovskite semiconductor has a high concentration of defects, it is expected that the single trap states located inside the energy bandgap will assist nonradiative recombination. Hence, the rate of change of carrier concentration, dn/dt, of a perovskite LED under lasing operation can be written as[113]

$$\frac{dn}{dt} = \frac{J}{qd} - \underbrace{\left(A_{nr}n + Bn^2 + Cn^3 + R_{st}(n)S_{ph}\right)}_{R(n)}, \qquad (1)$$

where n is the injected carrier concentration, J is the injection current density, q is the charge and d is the thickness of the emitting layer. $R(n)$ is the total recombination rate, the first term of $R(n)$, $A_{nr}n$, is the Shockley Read Hall (SRH) nonradiative recombination (ie, trap states assisted recombination), the second term of $R(n)$, Bn^2, is the spontaneous radiative recombination, the third term of $R(n)$, Cn^3, is the nonradiative Auger recombination (ie, collision between two similar carriers resulting in the transfer of kinetic energy) and the last term of $R(n)$, $R_{st}S_{ph}$, is the stimulated recombination and S_{ph} is the photon density. Previous investigation has shown that SRH recombination is dominant in $MAPbI_3$

film at room temperature for $n \leq 10^{15}$ cm^{-3}. Auger recombination starts to kick-in in the nonradiative recombination process for $n > 2 \times 10^{16}$ cm^{-3}.[114]

The rate equation of photons under the constraint of laser operation can be written as

$$\frac{dS_{ph}}{dt} = v_g(a_N(n-n_{tr})-\gamma)S_{ph} + \beta Bn^2, \quad (2)$$

where $R_{st}(n) \approx v_g a_N(n—n_{tr})$, a_N is the gain coefficient, and n_{tr} is the carrier concentration at transparent, v_g is the group velocity, γ is the cavity loss, and β spontaneous coupling coefficient. At the laser threshold, threshold carrier concentration, n_{th}, can be deduced from Equation (2) by equating cavity loss to the optical gain, we have

$$n_{th} = \frac{\gamma}{a_N} + n_{tr}, \quad (3)$$

This indicates that for the laser operating above the threshold, n will be clamped at n_{th} which is independent of the external injection of the carrier. Recent studies of $MAPbI_3$ DFB laser operating at 170 K has shown that $a_N \sim 10^{-16}$ cm^2, $n_{tr} \sim 4.5 \times 10^{18}$ cm^{-3}, and $\gamma = 70$ cm^{-1} so that the corresponding value of n_{th} is found to be about 5.2×10^{18} cm^{-3}.[39] This DFB laser has negligible Auger recombination so that SRH nonradiative recombination is still the dominant mechanism inside the $MAPbI_3$ film for $n_{th} < 6 \times 10^{18}$ cm^{-3}.

The excitation threshold, J_{th}, of the perovskite lasers can be deduced from Equation (1) by setting $n = n_{th}$ and the radiative recombination terms to zero, we have

$$J_{th} \simeq qdA_{nr}n_{th}, \quad (4)$$

where the influence of Auger recombination is ignored. Using the value of n_{th} obtained at 170 K, we found that $J_{th} \sim 149.8$ A/cm^2 for $d = 0.12$ μm and $A_{nr} \sim 1.5 \times 10^7$ s^{-1}.[39] For room-temperature operation, it is estimated that n_{th} of the $MAPbI_3$ DFB laser increases to ~2.6×10^{19} cm^{-3} and the corresponding J_{th} is 748.8 A/cm^2. It is noted that the excitation threshold of electrically pumped organic lasers is ~700 A/cm^2[45] and the injection current can go up to ~2k A/cm^2. Hence, this indicates that it is possible to achieve $MAPbI_3$ DFB laser diodes under ns pulses operation through using the carrier injection architecture of the organic laser diodes, and suppressing the influence of pump induced heating and the accumulation of photo-induced defects in $MAPBI_3$.[39] In this case, the influence of nonradiative recombination seems to be a manageable problem in perovskite lasers under electrical pulses excitation.

3.5 | Joule heating

It is believed that portion of external injected carriers that have not contributed to the light conversion will mostly lead to the generation of heat. This is the dominant factor causing the reduction of EQE and EQE roll-off of the electrically pumped lasers. For the laser diodes with a standard three-layer architecture, the corresponding heat sources are due to (a) the flow of charge carriers across the resistive media (ie, work done by the charge carriers traveling across the transport and emitting layers), (b) work done by the charge carriers over the barriers at the interfaces (ie, metal contact/ETL, ETL/emitting layer, emitting layer/HTL, HTL/metal contact), (c) phonons obtained from the nonradiative recombination at the emitting layer, and (d) the reabsorption of lasing light. Nevertheless, the heat distribution inside the laser diode can be described in a macroscopic view by using the time-dependent heat equation given as follows:

$$\rho_m C_p \frac{\partial T}{\partial t} = \nabla\cdot(\kappa_T \nabla T) + \rho_T, \quad (5)$$

where ρ_m (g/cm^3) is the mass density, C_p (J·g^{-1}·K^{-1}) is the heat capacity, κ_T (W·cm^{-1}·K^{-1}) is the thermal conductivity, and ρ_T (W/cm^3) is the power density. ρ_T is used to describe two major heat sources including (a) Joule heating due to the series electrical resistance of all the semiconductor layers inside the laser cavity, and (b) junction heating due to the heat generated from the emitting layer. We integrate Equation (5) over the cavity volume, V_s, between the heat sources and heatsink, which gives

$$C_T \frac{\partial T}{\partial t} = (P_{IV} - P) - \frac{T - T_o}{R_T}, \quad (6)$$

where T_o is the heatsink temperature, C_T ($=\rho_m C_p V_s$) is the thermal capacitance of the laser cavity. P_{IV} and P (W) are the total input electrical power and output optical power of the laser, respectively. R_T (K/W) is the equivalent thermal resistance which can be written as[115]

$$R_T = \frac{4}{Lw}\sum_i \frac{d_i}{\kappa_{T,i}}, \quad (7)$$

where i is the number of layers, L is the length, and w is the width of the laser cavity. d_i and $\kappa_{T,i}$ are the thickness and thermal conductivity of the ith layer, respectively. By setting n to n_{th} for $J > J_{th}$ in Equation (1), we have the output power, P, of the laser under CW operation:

$$P = A_{\text{eff}}(J - J_{\text{th}}(T))\cdot h\nu\cdot\eta_d\cdot q^{-1}, \tag{8}$$

where A_{eff} is the effective cross-sectional area of the laser cavity, η_{d} is the different quantum efficiency, h is the Plank's constant, and ν is the emission frequency. The operation temperature, T, of the laser can be calculated from $T = T_{\text{o}} + (P_{\text{IV}}—P)\cdot R_{\text{T}}$ where $P_{\text{IV}} \sim I^2R_{\text{s}} + IV_{\text{J}}$, I ($=L\cdot w\cdot J$) is current, R_{s} is the equivalent resistance, and V_{J} is the junction voltage of the emitting layer which can be approximated by[116]

$$V_J = E_g + \frac{IR_1}{T - T_1} + n_f \ln\left[1 + \frac{I}{I_1(T - T_1)}\right], \tag{9}$$

where E_{g} (=1.64 V), R_1 (=50 Ωκ), T_1 (=150 K), n_{f} (=0.02123468 V), and I_1 ($=3.907 \times 10^{-6}$ A/K) are the fitting parameters. The temperature dependence of $J_{\text{th}}(T)$ can be deduced from Equation (4) by using the temperature dependence of n_{th} for $MAPbI_3$ semiconductor films as[39]

$$n_{th} = n_{th,0}T^3\left(\cot^2(k_bT\pi/E_0) + 1\right), \tag{10}$$

where k_{b} is the Boltzmann's constant, $n_{\text{th,0}}$ ($=0.76 \times 10^{12}$ $\text{cm}^{-3}\cdot\text{K}^{-3}$) and E_0 (=0.038 eV) are the fitting parameters. From Equation (10), it is noted that the values of n_{th} as well as J_{th} increase with the increase of T, see Figure 4A. EQE roll-off of the laser diode can be expected from Equation (8) as the increase in J increases the heat generation through $(P_{\text{IV}}—P)\cdot R_{\text{T}}$ so that the value of J_{th} also increases. As a result, P reduces through the decrease of $(J—J_{\text{th}})$. In this case, we can suppress the generation of heat by reducing the values of R_{T} and $(P_{\text{IV}}—P)$ so that the kick-in of the EQE roll-off can be delayed at a higher value of J, see Figure 4B,C. These show that both R_{T} and $(P_{\text{IV}}—P)$ have a significant contribution to the EQE roll-off of the laser diodes.

From the above studies, it is noted that the Joule heating is the dominant factor and directly affects the conversion efficiency of the laser diodes. However, the amount of heat generation can be reduced by improving the heat dissipation inside the cavities through the reduction of R_{T}. This is equivalent to replace the materials of the laser diodes with a higher value of k_{T} but without changing the corresponding electrical and optical properties. Previous investigation has verified that the use of monocrystal Si as the substrate and as a charge injection layer instead of using ITO/glass substrate in perovskite LEDs can alleviate the influence of thermal effects.[94] This is because κ_{T} (~150 $\text{W}\cdot\text{m}^{-1}\cdot\text{K}^{-1}$) of monocrystal Si is much higher than that of glass (~1 $\text{W}\cdot\text{m}^{-1}\cdot\text{K}^{-1}$) at room temperature.[96] As expected from Equation (7), heat dissipates to the heatsink can be significantly enhanced using monocrystal Si substrate instead of glass so that only a slight increase of temperature from 28°C to 33°C is recorded. For LEDs using ITO/glass as the substrate, the increase in temperature can be up to 86°C.

Heat generation can also be suppressed by reducing the value of $(P_{\text{IV}}—P)$. This is equivalent to minimize the Joule heating inside the laser diode architecture as discussed above (ie, reduces the value of P_{IV}) or suppressing the nonradiative recombination in the emitting layer (ie, increase the value of P). A similar idea has suggested to reduce the resistivity of the CTLs and facilitate heat dissipation in perovskite LEDs.[96] They used doped ETL (ie, to increase conductivity from ~10^{-8} to ~10^{-2} $\text{S}\cdot\text{m}^{-1}$) and HTL (ie, to increase conductivity from ~0.01 to ~0.04 $\text{S}\cdot\text{m}^{-1}$) to reduce Joule heating of the device. The LED also has a narrow line-shape device geometry to reduce total power consumption and increase heat dissipation. These design strategies are equivalent to the reduction of P_{IV} in Equation (6). Furthermore, it is proposed to improve the heat dissipation by attaching an additional heat sink and diamond heat spreader ($\kappa_{\text{T}} > 2000$ $\text{W}\cdot\text{m}^{-1}\cdot\text{K}^{-1}$) on the top Ag contact of the LED. Furthermore, a sapphire substrate with better thermal conductivity is used to replace the bottom glass substrate of the LED. As expected from Equation (7), the total κ_{T} can be significantly reduced. As a result, the LED achieves EQE of 17% with a considerable reduction of EQE roll-off due to their proper thermal management. Hence, we have shown that the thermal effect has a direct impact on the performance of perovskite lasers and is unavoidable unless 100% of electrical-to-photon conversion efficiency can achieve.

4 | IDENTIFY CRITICAL PROBLEMS AND PROPOSE SOLUTIONS TO REALIZE PEROVSKITE LASER DIODES

4.1 | Critical issues

Table 1 estimates that the lowest excitation threshold at room temperature under pulses and CW operation of the DFB lasers are 7.5 kA/cm^2 and 8.17 A/cm^2, respectively. Table 3 shows the recently developed perovskite LEDs in which the carrier injection architectures can be used to excite the perovskite lasers. Unfortunately, the corresponding current density at the peak EQE is insufficient to sustain lasing from the DFB lasers at room temperature. Further increase of current density for the perovskite LEDs is possible but at the expense of EQE roll-off. This is because the portion of electrical power

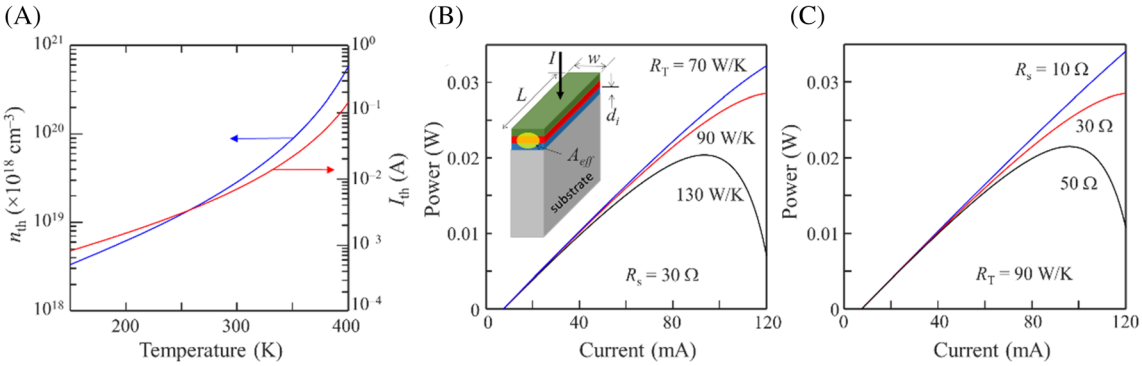

FIGURE 4 A, Plot of threshold carrier concentration, n_{th}, and threshold current, I_{th}, vs temperature by using Equation (10). Plots of output power vs input current by using Equation (8) for different values of, B, R_T and, C, R_s under continuous-wave (CW) operation. The schematic diagram inset in, B, is the configuration of the laser diode. The heatsink temperature, T_o, is set to 300 K

not contributed to light generation will lead to "heating," and the temperature will increase with the increase of injection current. From the previous study on the heat generation in LEDs under CW operation, the increase in temperature can be as much as ~20°C per 100 mA/cm^2.[94] Therefore, heating is the main problem for using the available LED architectures as an excitation source. On the other hand, it is noted that the threshold carrier concentration, n_{th} ($=\gamma/a_N + n_{tr}$), /or /the threshold current density (ie, $J_{th} \propto n_{th}$) is dependent on the design of laser cavities (ie, γ) as well as the transparency carrier concentration, n_{tr}, of the perovskite semiconductors. From the above study, the value of γ/a_N is in the same order of magnitude as that of n_{tr} (ie, based on $MAPbI_3$[39]) so that even if the cavity loss, γ, decreases to zero, the threshold current can only be reduced by 50%. As a result, the injection current below J_{th} contributes to the non-radiative recombination of carriers and generates heat—pump-induced heating.[39] It must be noted that n_{tr} is an intrinsic property of perovskite semiconductors and cannot be changed by improving its crystal quality so that this inherent heating effect of perovskite lasers cannot be avoided. Hence, the main challenges to achieve electrically pumped perovskite DFB lasers can now be focused on two issues: (a) How to minimize the "heating effect" from the LED architectures under CW operation at high current density? (b) How to further reduce the excitation threshold to suppress pump-induced heating?

The VCSELs shown in Table 1 have the lowest threshold current of 314 A/cm^2 and 24 mA/cm^2 for the device in pulses and CW operation, respectively, which can theoretically be utilized to suppress pump-induced heating. It is noted that the perovskite LED architectures can provide enough current to excite the VCSELs at room temperature under either pulses or CW operation although the operation of the pulse of $MAPbBr_3$ LEDs has not been investigated. Nevertheless, the current design of VCSELs is not compatible with the LED architectures. This is because the insulating characteristics of DBRs, which are made by 13.5 pairs of alternating TiO_2/SiO_2 dielectric layers (ie, 3 μm thick), block the external injection of carriers. Even the DBRs can conduct electricity (eg, using low-index GaN/GaN dielectric layers), the large size of DBRs gives a large value of thermal resistance R_T. The low conductivity of the DBRs will also give a large value of equivalent resistance R_s so that strong Joule heating is unavoidable.[117] As we can see from Figure 4B,C, either the increase of R_T, R_s, or both will have a significant contribution to the EQE roll-off. Hence, the main challenges to achieve electrically pumped perovskite VCSELs can now be focused on two issues: (a) How to integrate the LED architecture with the VCSEL? (b) How to further reduce Joule heating and pump-induced heating for CW operation at room temperature.

4.2 | Proposed solutions

Perovskite semiconductors are suitable materials to realize polariton lasing because of their high excitonic binding energy and large exciton oscillator strength. So far, room-temperature optically pumped polariton lasing has been demonstrated from VCSELs,[118, 119] microcuboids,[120] and NWs[29] using perovskite semiconductor as the photon-exciton coupling region. The advantage of achieving polariton lasing is the immediate decay of polariton condensation to generate coherent monochromatic light so that no population inversion is required (ie, zero threshold for ideal polariton lasers). Hence, only a small amount of excitation power is enough to turn on the polariton lasers so that pump-induced heating can

be significantly suppressed. However, this is not straightforward to realize polariton lasers when compared to that of the conventional FP or DFB lasers as the strong coupling between excitons and photons within a small volume is required to achieve polariton condensation through the stimulated polariton-polariton scattering.[43]

Here, we propose to realize electrically pumped perovskite polariton lasers by adopting the design from a room-temperature GaN-based electrically pumped polariton lasers.[121, 122] This GaN polariton laser has a VCSEL structure where a thin GaN semiconductor layer is sandwiched between two Bragg reflectors. However, electrodes are not established between the two Bragg reflectors as in the conventional design of VCSELs, instead, the electrical current is injected into the emitting layer in the direction orthogonal to the path of optical feedback (ie, side injection). This laser configuration avoids the injection of carriers through the Bragg reflectors so that Joule heating is mainly dependent on the design of the LED architecture. To realize perovskite polariton lasers, we can replace the GaN layer with a perovskite semiconductor film such as $MAPbBr_3$. A standard LED architecture such as NiO_x/$MAPbBr_3$/TPBI can also be used to side-inject electrons and holes to the perovskite semiconductor, in the direction perpendicular to the optical feedback of the resonator, shown in Figure 5. The Joule heating of the LED architecture can be further reduced if doping can be introduced to the CTLs to reduce R_s. Furthermore, the diamond substrate can be used to reduce R_T of the LED architecture. Hence, the reduction of R_s and R_T allows the room-temperature CW operation of LED architecture to deliver high current. Hopefully, this suggestion can overcome the "two issues" affecting the development of electrically pumped perovskite lasers.

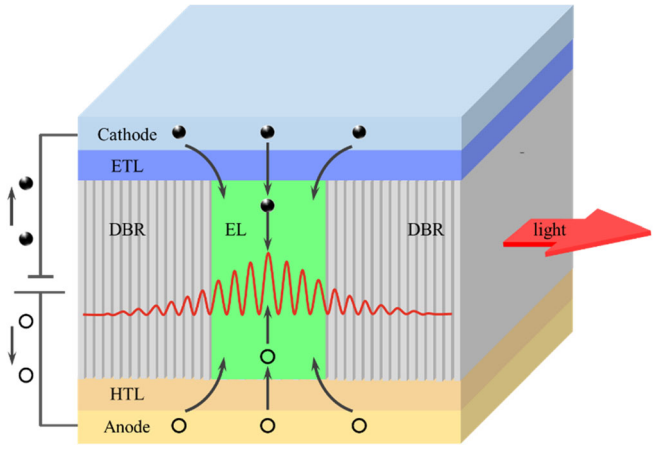

FIGURE 5 Proposed electrically pumped perovskite semiconductor laser. In this case, NiO_x is the hole-transport layer (HTL), TPBI is the electron-transport layer (ETL) and $MAPbBr_3$ is the emitting layer (EL). As we can see, the external injection of carriers is achieved via side injection to the EL. Lasing light is observed from the two end surfaces of the DBRs

5 | CONCLUSION

Even the standard three-layer LED architecture can generate a current density larger than the equivalent excitation threshold of the optically pumped perovskite lasers, it is still not guaranteed to support lasing emission. This is because the strong confinement of light within the emitting layer is not required for the design of LEDs. However, it is a must to simultaneously obtain strong confinement of carriers and photons within the emitting layer of the lasers to achieve stimulated emission. Furthermore, the emitting layer should behave like an optical waveguide collaborating with optical feedback (ie, FP or DFB structure) to generate coherent lasing light. Hence, in the design of standard three-layer LED architecture for laser applications, it is necessary to use CTLs with a refractive index lower than that of the emitting layer so that strong confinement of carriers and photons can be obtained simultaneously. On the other hand, for the design of VCSELs, the refractive index of the emitting layer should also be higher than that of the CTLs for the same reason. These imply that the available design of LED architectures may not be suitable for laser application so that the special design of external carrier injection was used to realize electrically pumped organic lasers.[45] Hence, careful redesign of the LED architectures is also required for the fabrication of perovskite laser diodes. In conclusion, it is believed that we are not far from achieving electrically pumped perovskite lasers—(a) based on the successful realization of electrically pumped organic semiconductor lasers reported recently, (b) our investigations on the electrical, thermal and optical properties of perovskite semiconductor materials, as well as (c) our understanding on the optical and electrical characteristics of the optically pumped perovskite lasers and perovskite LEDs, respectively.

ACKNOWLEDGMENTS

This work was supported by the National Natural Science Foundation of China, grant No. 61775187, and HK PolyU grants (Grant Nos. 1-BBA5, G-YBHG, 1-ZVGH, and BCEE).

ORCID

Siu Fung Yu https://orcid.org/0000-0003-0354-3767

REFERENCES

1. Wells HL. ART. XVI. On the caesium-and the potassium-lead halides. *Am J Sci*. 1893;45(266):121.
2. Book. Synthesis, structure, and properties of organic-inorganic perovskites and related materials. *Prog Inorg Chem*. 1999;48:1-121.
3. Mitzi DB, Chondroudis K, Kagan CR. Design, structure, and optical properties of organic–inorganic perovskites containing an oligothiophene chromophore. *Inorg Chem*. 1999;38(26):6246-6256.
4. Shi D, Adinolfi V, Comin R, et al. Solar cells. Low trap-state density and long carrier diffusion in organolead trihalide perovskite single crystals. *Science*. 2015;347(6221):519-522.
5. Wehrenfennig C, Liu M, Snaith HJ, Johnston MB, Herz LM. Charge-carrier dynamics in vapour-deposited films of the organolead halide perovskite CH3NH3PbI3−xClx. *Energ Environ Sci*. 2014;7(7):2269-2275.
6. Mitzi DB, Feild CA, Harrison WTA, Guloy AM. Conducting tin halides with a layered organic-based perovskite structure. *Nature*. 1994;369(6480):467-469.
7. Cao X, Zhi L, Jia Y, et al. A review of the role of solvents in formation of high-quality solution-processed perovskite films. *ACS Appl Mater Interfaces*. 2019;11(8):7639-7654.
8. Brenner P, Fleig LM, Liu X, Welle A, Brase S, Lemmer U. Degradation mechanisms of polyfluorene-based organic semiconductor lasers under ambient and oxygen-free conditions. *J Polym Sci Polym Phys*. 2015;53(15):1029-1034.
9. Stylianakis MM, Maksudov T, Panagiotopoulos A, Kakavelakis G, Petridis K. Inorganic and hybrid Perovskite based laser devices: a review. *Materials (Basel)*. 2019;12(6):859.
10. Ambrosio F, Wiktor J, de Angelis F, Pasquarello A. Origin of low electron–hole recombination rate in metal halide perovskites. *Energ Environ Sci*. 2018;11(1):101-105.
11. Brenner TM, Egger DA, Kronik L, Hodes G, Cahen D. Hybrid organic—inorganic perovskites: low-cost semiconductors with intriguing charge-transport properties. *Nat Rev Mater*. 2016;1(1):15007.
12. Dong H, Zhang C, Liu X, Yao J, Zhao YS. Materials chemistry and engineering in metal halide perovskite lasers. *Chem Soc Rev*. 2020;49(3):951-982.
13. Chi W, Banerjee SK. Progress in materials development for the rapid efficiency advancement of perovskite solar cells. *Small*. 2020;16:e1907531.
14. Qiu Z, Li N, Huang Z, Chen Q, Zhou H. Recent advances in improving phase stability of perovskite solar cells. *Small Methods*. 2020;4(5):1900877.
15. Zheng Z, Hu Q, Zhou H, et al. Submillimeter and lead-free Cs3Sb2Br9 perovskite nanoflakes: inverse temperature crystallization growth and application for ultrasensitive photodetectors. *Nanoscale Horiz*. 2019;4(6):1372-1379.
16. Yang D, Huo D. Cation doping and strain engineering of CsPbBr3-based perovskite light emitting diodes. *J Mater Chem A*. 2020;8(20):6640-6653.
17. Philippe B, Jacobsson TJ, Correa-Baena J-P, et al. Valence level character in a mixed perovskite material and determination of the valence band maximum from photoelectron spectroscopy: variation with photon energy. *J Phys Chem C*. 2017;121(48):26655-26666.
18. de Quilettes DW, Vorpahl SM, Stranks SD, et al. Impact of microstructure on local carrier lifetime in perovskite solar cells. *Science*. 2015;348(6235):683-686.
19. Quan LN, Rand BP, Friend RH, Mhaisalkar SG, Lee T-W, Sargent EH. Perovskites for next-generation optical sources. *Chem Rev*. 2019;119(12):7444-7477.
20. Xing G, Mathews N, Lim SS, et al. Low-temperature solution-processed wavelength-tunable perovskites for lasing. *Nat Mater*. 2014;13(5):476-480.
21. Fujiwara K, Zhang S, Takahashi S, Ni L, Rao A, Yamashita K. Excitation dynamics in layered lead halide perovskite crystal slabs and microcavities. *ACS Photonics*. 2020;7(3):845-852.
22. Wang X, Chen H, Zhou H, et al. Room-temperature high-performance CsPbBr3 perovskite tetrahedral microlasers. *Nanoscale*. 2019;11(5):2393-2400.
23. Li C, Zang Z, Han C, et al. Highly compact CsPbBr3 perovskite thin films decorated by ZnO nanoparticles for enhanced random lasing. *Nano Energy*. 2017;40:195-202.
24. Pourdavoud N, Mayer A, Buchmüller M, et al. Distributed feedback lasers based on MAPbBr3. *Adv Mater Technol*. 2018;3(4):1700253.
25. Park K, Lee JW, Kim JD, et al. Light–matter interactions in cesium lead halide perovskite nanowire lasers. *J Phys Chem Lett*. 2016;7(18):3703-3710.
26. Zhu H, Fu Y, Meng F, et al. Lead halide perovskite nanowire lasers with low lasing thresholds and high quality factors. *Nat Mater*. 2015;14(6):636-642.
27. Jia Y, Kerner RA, Grede AJ, Rand BP, Giebink NC. Continuous-wave lasing in an organic–inorganic lead halide perovskite semiconductor. *Nat Photon*. 2017;11(12):784-788.
28. Brenner P, Bar-On O, Jakoby M, et al. Continuous wave amplified spontaneous emission in phase-stable lead halide perovskites. *Nat Commun*. 2019;10(1):988.
29. Evans TJS, Schlaus A, Fu Y, et al. Continuous-wave lasing in cesium lead bromide perovskite nanowires. *Adv Opt Mater*. 2018;6(2):1700982.
30. Li Z, Moon J, Gharajeh A, et al. Room-temperature continuous-wave operation of organometal halide perovskite lasers. *ACS Nano*. 2018;12(11):10968-10976.
31. Tian C, Tong G, Zhao S, Zhai W, Ge C, Ran G. Low-threshold room-temperature continuous-wave optical lasing of single-crystalline perovskite in a distributed reflector microcavity. *RSC Adv*. 2019;9(62):35984-35989.
32. Qin C, Sandanayaka ASD, Zhao C, et al. Stable room-temperature continuous-wave lasing in quasi-2D perovskite films. *Nature*. 2020;585(7823):53-57.
33. Wang Y, Li X, Song J, Xiao L, Zeng H, Sun H. All-inorganic colloidal perovskite quantum dots: a new class of lasing materials with favorable characteristics. *Adv Mater*. 2015;27(44):7101-7108.
34. Fu Y, Zhu H, Stoumpos CC, et al. Broad wavelength tunable robust lasing from single-crystal nanowires of cesium lead halide perovskites (CsPbX3, X = Cl, Br, I). *ACS Nano*. 2016;10(8):7963-7972.
35. Chen S, Zhang C, Lee J, Han J, Nurmikko A. High-Q, low-threshold monolithic perovskite thin-film vertical-cavity lasers. *Adv Mater*. 2017;29(16):1604781.
36. Gharajeh A, Haroldson R, Li Z, et al. Continuous-wave operation in directly patterned perovskite distributed feedback light source at room temperature. *Opt Lett*. 2018;43(3):611-614.

37. Jiang L, Liu R, Su R, et al. Continuous wave pumped single-mode nanolasers in inorganic perovskites with robust stability and high quantum yield. *Nanoscale*. 2018;10(28):13565-13571.
38. Wang L, Meng L, Chen L, et al. Ultralow-threshold and color-tunable continuous-wave lasing at room-temperature from in situ fabricated perovskite quantum dots. *J Phys Chem Lett*. 2019;10(12):3248-3253.
39. Jia Y, Kerner RA, Grede AJ, Rand BP, Giebink NC. Factors that limit continuous-wave lasing in hybrid perovskite semiconductors. *Adv Opt Mater*. 2019;8(2):1901514.
40. Chénais S, Forget S. Recent advances in solid-state organic lasers. *Polym Int*. 2012;61(3):390-406.
41. Yokoyama D, Moriwake M, Adachi C. Spectrally narrow emissions at cutoff wavelength from edges of optically and electrically pumped anisotropic organic films. *J Appl Phys*. 2008;103(12):123104.
42. Liu X, Li H, Song C, Liao Y, Tian M. Microcavity organic laser device under electrical pumping. *Opt Lett*. 2009;34(4):503-505.
43. Du W, Zhang S, Zhang Q, Liu X. Recent progress of strong exciton–photon coupling in lead halide perovskites. *Adv Mater*. 2019;31(45):1804894.
44. Sandanayaka ASD, Matsushima T, Bencheikh F, et al. Toward continuous-wave operation of organic semiconductor lasers. *Sci Adv*. 2017;3(4):e1602570.
45. Sandanayaka ASD, Matsushima T, Bencheikh F, et al. Indication of current-injection lasing from an organic semiconductor. *Appl Phys Express*. 2019;12(6):061010.
46. Cho H, Wolf C, Kim JS, et al. High-efficiency solution-processed inorganic metal halide perovskite light-emitting diodes. *Adv Mater*. 2017;29(31):1700579.
47. Kang Y, Han S. Intrinsic carrier mobility of cesium lead halide perovskites. *Phys Rev Appl*. 2018;10(4):044013.
48. Yang Z, Xu Q, Wang X, et al. Large and ultrastable all-inorganic CsPbBr3 monocrystalline films: low-temperature growth and application for high-performance photodetectors. *Adv Mater*. 2018;30(44):e1802110.
49. He Y, Galli G. Perovskites for solar thermoelectric applications: a first principle study of CH3NH3AI3(A = Pb and Sn). *Chem Mater*. 2014;26(18):5394-5400.
50. Onoda-Yamamuro N, Matsuo T, Suga H. Calorimetric and IR spectroscopic studies of phase transitions in methylammonium trihalogenoplumbates (II)†. *J Phys Chem Solid*. 1990;51(12):1383-1395.
51. Frost JM. Calculating polaron mobility in halide perovskites. *Phys Rev B*. 2017;96(19):195202.
52. Ye T, Wang X, Li X, Yan AQ, Ramakrishna S, Xu J. Ultra-high Seebeck coefficient and low thermal conductivity of a centimeter-sized perovskite single crystal acquired by a modified fast growth method. *J Mater Chem C*. 2017;5(5):1255-1260.
53. Pisoni A, Jaćimović J, Barišić OS, et al. Ultra-low thermal conductivity in organic–inorganic hybrid perovskite CH3NH3PbI3. *J Phys Chem Lett*. 2014;5(14):2488-2492.
54. A Y, M B, X B, J W, W Z. Investigation of optical and dielectric constants of organic-inorganic CH3NH3PbI3 perovskite thin films. *J Nanomed Nanotechnol*. 2016;07(05):1000407.
55. Bencheikh F, Sandanayaka ASD, Fukunaga T, Matsushima T, Adachi C. Origin of external quantum efficiency roll-off in 4,4′-bis[(N-carbazole)styryl]biphenyl (BSBCz)-based inverted organic light emitting diode under high pulsed electrical excitation. *J Appl Phys*. 2019;126(18):185501.
56. Takashi ACSSDAMTYKRJ-CFBGKF, inventor; Continuous-wave organic thin-film distributed feedback laser and electrically driven organic semiconductor laser diode. Patent application WO2017JP33366 20170901; 2018.
57. Mamada M, Fukunaga T, Bencheikh F, Sandanayaka ASD, Adachi C. Low amplified spontaneous emission threshold from organic dyes based on bis-stilbene. *Adv Funct Mater*. 2018;28(32):1802130.
58. Sze SM, Ng KK. *Physics of semiconductor devices*. Hoboken, New Jersey: John Wiley & Sons; 2006. https://www.wiley.com/en-hk/Physics+of+Semiconductor+Devices,+3rd+Edition-p-9780471143239.
59. Harafuji K, Tsuchiya T, Kawamura K. Molecular dynamics simulation for evaluating melting point of wurtzite-type GaN crystal. *J Appl Phys*. 2004;96(5):2501-2512.
60. Wu X, Lee J, Varshney V, Wohlwend JL, Roy AK, Luo T. Thermal conductivity of wurtzite zinc-oxide from first-principles lattice dynamics—a comparative study with gallium nitride. *Sci Rep*. 2016;6:22504.
61. Bandić ZZ, Bridger PM, Piquette EC, McGill TC. Minority carrier diffusion length and lifetime in GaN. *Appl Phys Lett*. 1998;72(24):3166-3168.
62. Porowski S, Bockowski M, Lucznik B, et al. High resistivity GaN single crystalline substrates. *Acta Phys Polym A*. 1997;92(5):958-962.
63. Takahashi K, Yoshikawa A, Sandhu A. *Wide Bandgap Semiconductors*. Berlin, Heidelberg: Springer; 2007. https://www.springer.com/gp/book/9783540472346.
64. Karninska E, Piotrowska A, Golaszewska K, et al. Engineering ZnO/GaN interfaces for tunneling ohmic contacts to GaN. *Mater Res Soc Symp P*. 2003;747:353-358.
65. Materials A. Diamond (C)—Properties and Applications. https://www.azom.com/article.aspx?ArticleID=262. Accessed August 22, 2020.
66. Ahmad M, Rehman G, Ali L, et al. Structural, electronic and optical properties of CsPbX3 (X=Cl, Br, I) for energy storage and hybrid solar cell applications. *J Alloys Compd*. 2017;705:828-839.
67. Oyama Y, Mamada M, Shukla A, et al. Design strategy for robust organic semiconductor laser dyes. *ACS Mater Lett*. 2020;2(2):161-167.
68. Setoguchi Y, Adachi C. Suppression of roll-off characteristics of electroluminescence at high current densities in organic light emitting diodes by introducing reduced carrier injection barriers. *J Appl Phys*. 2010;108(6):064516.
69. Sutherland BR, Hoogland S, Adachi MM, et al. Perovskite thin films via atomic layer deposition. *Adv Mater*. 2015;27(1):53-58.
70. Aimono T, Kawamura Y, Goushi K, Yamamoto H, Sasabe H, Adachi C. 100% fluorescence efficiency of 4,4[sup ′]-bis[(N-carbazole)styryl]biphenyl in a solid film and the very low amplified spontaneous emission threshold. *Appl Phys Lett*. 2005;86(7):071110.
71. Hoye RLZ, Chua MR, Musselman KP, et al. Enhanced performance in fluorene-free organometal halide perovskite light-emitting diodes using tunable, low electron affinity oxide electron injectors. *Adv Mater*. 2015;27(8):1414-1419.

72. Kwak J, Bae WK, Lee D, et al. Bright and efficient full-color colloidal quantum dot light-emitting diodes using an inverted device structure. *Nano Lett*. 2012;12(5):2362-2366.
73. Zhang X, Sun C, Zhang Y, et al. Bright perovskite nanocrystal films for efficient light-emitting devices. *J Phys Chem Lett*. 2016;7(22):4602-4610.
74. Gao Z, Lee CS, Bello I, et al. Bright-blue electroluminescence from a silyl-substituted ter-(phenylene–vinylene) derivative. *Appl Phys Lett*. 1999;74(6):865-867.
75. Zhang X, Zhang Y, Yan L, et al. High photocurrent PbSe solar cells with thin active layers. *J Mater Chem A*. 2015;3(16):8501-8507.
76. Zhang Z, Zhang Z, Ye K, Zhang J, Zhang H, Wang Y. Diboron complexes with bis-spiro structures as high-performance blue emitters for OLEDs. *Dalton Trans*. 2015;44(32):14436-14443.
77. Zhang X, Lin H, Huang H, et al. Enhancing the brightness of cesium lead halide perovskite nanocrystal based green light-emitting devices through the interface engineering with perfluorinated ionomer. *Nano Lett*. 2016;16(2):1415-1420.
78. Chih Y-K, Wang J-C, Yang R-T, et al. NiOx electrode interlayer and CH3NH2/CH3NH3PbBr3 interface treatment to markedly advance hybrid perovskite-based light-emitting diodes. *Adv Mater*. 2016;28(39):8687-8694.
79. Wang J, Wang N, Jin Y, et al. Interfacial control toward efficient and low-voltage perovskite light-emitting diodes. *Adv Mater*. 2015;27(14):2311-2316.
80. Tan ZK, Moghaddam RS, Lai ML, et al. Bright light-emitting diodes based on organometal halide perovskite. *Nat Nanotechnol*. 2014;9(9):687-692.
81. Kabra D, Lu LP, Song MH, Snaith HJ, Friend RH. Efficient single-layer polymer light-emitting diodes. *Adv Mater*. 2010;22(29):3194-3198.
82. Mahmood K, Swain BS, Amassian A. 16.1% efficient hysteresis-free mesostructured perovskite solar cells based on synergistically improved ZnO nanorod arrays. *Adv Energy Mater*. 2015;5(17):1500568.
83. Saracco E, Bouthinon B, Verilhac J-M, et al. Work function tuning for high-performance solution-processed organic photodetectors with inverted structure. *Adv Mater*. 2013;25(45):6534-6538.
84. Weber C, Oberberg M, Weber D, Bock C, Pham DV, Kunze U. Improved morphology and performance of solution-processed metal-oxide thin-film transistors due to a polymer based Interface modifier. *Adv Mater Interfaces*. 2014;1(7):1400137.
85. Yin J, Ahmed GH, Bakr OM, Brédas J-L, Mohammed OF. Unlocking the effect of trivalent metal doping in all-inorganic CsPbBr3 perovskite. *ACS Energy Lett*. 2019;4(3):789-795.
86. Bi C, Wang S, Li Q, Kershaw SV, Tian J, Rogach AL. Thermally stable copper(II)-doped cesium lead halide perovskite quantum dots with strong blue emission. *J Phys Chem Lett*. 2019;10(5):943-952.
87. Lin K, Xing J, Quan LN, et al. Perovskite light-emitting diodes with external quantum efficiency exceeding 20 per cent. *Nature*. 2018;562(7726):245-248.
88. Sun S, Salim T, Mathews N, et al. The origin of high efficiency in low-temperature solution-processable bilayer organometal halide hybrid solar cells. *Energ Environ Sci*. 2014;7(1):399-407.
89. Song J, Li J, Li X, Xu L, Dong Y, Zeng H. Quantum dot light-emitting diodes based on inorganic perovskite cesium lead halides (CsPbX3). *Adv Mater*. 2015;27(44):7162-7167.
90. Kim Y-H, Cho H, Heo JH, et al. Multicolored organic/inorganic hybrid perovskite light-emitting diodes. *Adv Mater*. 2015;27(7):1248-1254.
91. Cho H, Jeong SH, Park MH, et al. Overcoming the electroluminescence efficiency limitations of perovskite light-emitting diodes. *Science*. 2015;350(6265):1222-1225.
92. Song L, Guo X, Hu Y, et al. Improved performance of CsPbBr3 perovskite light-emitting devices by both boundary and interface defects passivation. *Nanoscale*. 2018;10(38):18315-18322.
93. Simkus G, Sanders S, Stümmler D, Vescan A, Kalisch H, Heuken M. High-intensity CsPbBr3 perovskite LED using poly(bis(4-phenyl)(2,4,6-trimethylphenyl)amine) as hole transport and electron-blocking layer. *MRS Adv*. 2020;5(8–9):411-419.
94. Xu H, Wang X, Li Y, et al. Prominent heat dissipation in perovskite light-emitting diodes with reduced efficiency droop for silicon-based display. *J Phys Chem Lett*. 2020;11(9):3689-3698.
95. Cao Y, Wang N, Tian H, et al. Perovskite light-emitting diodes based on spontaneously formed submicrometre-scale structures. *Nature*. 2018;562(7726):249-253.
96. Zhao L, Roh K, Kacmoli S, et al. Thermal management enables bright and stable perovskite light-emitting diodes. *Adv Mater*. 2020;32(25):2000752.
97. Young RH, Tang CW, Marchetti AP. Current-induced fluorescence quenching in organic light-emitting diodes. *Appl Phys Lett*. 2002;80(5):874-876.
98. Han Y, Lee SS, Ying JY. Spherical siliceous mesocellular foam particles for high-speed size exclusion chromatography. *Chem Mater*. 2007;19(9):2292-2298.
99. Popovic ZD, Menzel ER. Electric field-induced fluorescence quenching in organic photoconductors. *J Chem Phys*. 1979;71(12):5090-5096.
100. Cheng L, Jiang T, Cao Y, et al. Multiple-quantum-well perovskites for high-performance light-emitting diodes. *Adv Mater*. 2020;32(15):1904163.
101. Akselrod GM, Tischler YR, Young ER, Nocera DG, Bulovic V. Exciton-exciton annihilation in organic polariton microcavities. *Phys Rev B*. 2010;82(11):113106.
102. Yuan F, Wu Z, Dong H, et al. Electric field-modulated amplified spontaneous emission in organo-lead halide perovskite CH3NH3PbI3. *Appl Phys Lett*. 2015;107(26):261106.
103. Kattoor V, Awasthi K, Jokar E, Diau EW-G, Ohta N. Enhanced dissociation of hot excitons with an applied electric field under low-power photoexcitation in two-dimensional perovskite quantum wells. *J Phys Chem Lett*. 2019;10(16):4752-4757.
104. Xia S, Wang Z, Ren Y, Gu Z, Wang Y. Unusual electric field-induced optical behaviors in cesium lead bromide perovskites. *Appl Phys Lett*. 2019;115(20):201101.
105. Zou W, Li R, Zhang S, et al. Minimising efficiency roll-off in high-brightness perovskite light-emitting diodes. *Nat Commun*. 2018;9(1):608.
106. Kim H, Zhao L, Price JS, et al. Hybrid perovskite light emitting diodes under intense electrical excitation. *Nat Commun*. 2018;9(1):4893.
107. Ahn N, Kwak K, Jang MS, et al. Trapped charge-driven degradation of perovskite solar cells. *Nat Commun*. 2016;7(1):13422.
108. Lee J-W, Kim S-G, Yang J-M, Yang Y, Park N-G. Verification and mitigation of ion migration in perovskite solar cells. *APL Materials*. 2019;7(4):041111.

109. Queisser HJ, Haller EE. Defects in semiconductors: some fatal, some vital. *Science*. 1998;281(5379):945-950.
110. Ball JM, Petrozza A. Defects in perovskite-halides and their effects in solar cells. *Nat Energy*. 2016;1(11):1-13.
111. Wang F, Bai S, Tress W, Hagfeldt A, Gao F. Defects engineering for high-performance perovskite solar cells. *npj Flex Electron*. 2018;2(1):22.
112. Han T-H, Tan S, Xue J, Meng L, Lee J-W, Yang Y. Interface and defect engineering for metal halide perovskite optoelectronic devices. *Adv Mater*. 2019;31(47):1803515.
113. Chuang SL. *Physics of Photonic Devices*. Vol 2nd. Hoboken, NJ: John Wiley & Sons; 2012. https://www.wiley.com/en-hk/Physics+of+Photonic+Devices,+2nd+Edition-p-9780470293195.
114. Brakkee R, Williams RM. Minimizing defect states in lead halide perovskite solar cell materials. *Appl Sci*. 2020;10(9):3061.
115. Yu SF. Thermal characteristics of vertical cavity surface emitting lasers. *Analysis and Design of Vertical Cavity Surface Emitting Lasers*. Hoboken, NJ: John Wiley & Sons, Inc.; 2003;193-227.
116. Mena PV, Morikuni JJ, Kang S, Harton AV, Wyatt KW. A comprehensive circuit-level model of vertical-cavity surface-emitting lasers. *J Light Technol*. 1999;17(12):2612-2632.
117. Era M, Morimoto S, Tsutsui T, Saito S. Organic-inorganic heterostructure electroluminescent device using a layered perovskite semiconductor (C6H5C2H4NH3)2PbI4. *Appl Phys Lett*. 1994;65(6):676-678.
118. Su R, Diederichs C, Wang J, et al. Room-temperature polariton lasing in all-inorganic perovskite nanoplatelets. *Nano Lett*. 2017;17(6):3982-3988.
119. Wang J, Su R, Xing J, et al. Room temperature coherently coupled exciton–polaritons in two-dimensional organic–inorganic perovskite. *ACS Nano*. 2018;12(8):8382-8389.
120. Han Q, Wang J, Lu J, et al. Transition between exciton-polariton and coherent photonic lasing in all-inorganic perovskite microcuboid. *ACS Photonics*. 2020;7(2):454-462.
121. Bhattacharya P, Frost T, Deshpande S, Baten MZ, Hazari A, Das A. Room temperature electrically injected polariton laser. *Phys Rev Lett*. 2014;112(23):236802.
122. Savvidis PG. A practical polariton laser. *Nat Photon*. 2014;8(8):588-589.
123. Wenger B, Nayak PK, Wen X, Kesava SV, Noel NK, Snaith HJ. Consolidation of the optoelectronic properties of CH3NH3PbBr3 perovskite single crystals. *Nat Commun*. 2017;8(1):590.
124. Leguy AMA, Azarhoosh P, Alonso MI, et al. Experimental and theoretical optical properties of methylammonium lead halide perovskites. *Nanoscale*. 2016;8(12):6317-6327.

AUTHOR BIOGRAPHIES

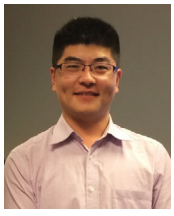

Wei Gao is currently a PhD candidate under the supervision of Prof S. F. Y. in the Department of Applied Physics, the Hong Kong Polytechnic University, China. He received his MPhil degree in Chemistry from the Hong Kong Polytechnic University in 2019. His current research focuses on the optical properties of various materials, including semiconductors, organic materials, perovskites, and rare-earth metal-doped materials, and their promising applications in realizing microlasers with the high conversion efficiency.

Siu Fung Yu received B(Eng) degree from University College London, England in 1990 and a PhD degree from Cambridge University, England in 1993. He is now a professor in the Department of Applied Physics, the Hong Kong Polytechnic University, China. His main research interest includes fundamental study, design, and optimization of lasers. He has led to the first realization of random laser diodes, carbon nanodots lasers, and rare-earth-doped nanoparticles upconversion lasers. He has published over 400 international technical papers including patents, journal and conference papers, five book chapters, and one book entitled "Analysis and Design of Vertical-Cavity Surface-Emitting Lasers," 2003 Wiley, NY.

How to cite this article: Gao W, Yu SF. Reality or fantasy—Perovskite semiconductor laser diodes. *EcoMat*. 2021;3:e12077. https://doi.org/10.1002/eom2.12077

APPENDIX

The pumping rate, R_p (cm^{-3} s^{-1}) for optical and electrical excitation can be written as

$$R_p = \eta_p \frac{\lambda_{ex} n}{dhc} P\left(1 - e^{-\alpha d}\right) \equiv \eta_J \frac{J}{qd}, \tag{A1}$$

where η_p is the pump efficiency, h is the Planck's constant, c is the velocity of light, λ_{ex} is the excitation wavelength, n is the refractive index, d is the active layer thickness, α is the absorption coefficient at λ_{ex}, P is the excitation power, q is the charge, and J is the equivalent current density. Using Reference 31 as an example, for the laser under pulses excitation with pulses energy and pulse width of 4 μJ/cm^2 and 8 ns, respectively, then $P = 4 \times 10^{-6}/8 \times 10^{-9} = 500$ W/cm^2. Furthermore, using $\lambda_{ex} = 355$ nm, $n = 2.2$,[123] $d = 1$ μm, $\alpha = 2 \times 10^5$ cm^{-1},[124] and with the assumption of $\eta_p \sim \eta_J$, we obtain

$J = 314.3$ A/cm^2 which is a peak value of current pulses. On the other hand, if CW excitation is used, and setting $P = 34$ mW/cm^2, and $\alpha = 1 \times 10^5$ cm^{-1} @ $\lambda_{ex} \sim 400$ nm so that $J = 21.4$ mA/cm^2 which is the CW excitation current. In general, it is assumed that α of $MAPbBr_3$ is equal to 2×10^5, 1×10^5, and 0.7×10^5 cm^{-1} for λ_{ex} at 355, 400, and 530 nm, respectively. Furthermore, α of $MAPbI_3$ is assumed equal to 6×10^5, 1×10^5, and 0.6×10^5 cm^{-1} for λ_{ex} at 335, 400, and 600 nm, respectively. For $FAPbBr_3$, the value of α is assumed equal to 6×10^5 cm^{-1}. These parameters are used to calculate the threshold current given in Table 1.